

Article

The Relationship between Solar Wind Charge Exchange Soft X-ray Emission and the Tangent Direction of Magnetopause in an XMM–Newton Event

Yingjie Zhang ^{1,2}, Tianran Sun ^{1,*}, Jennifer A. Carter ³, Wenhao Liu ⁴, Steve Sembay ³, Li Ji ⁴
and Chi Wang ^{1,2,*}

- ¹ State Key Laboratory of Space Weather, National Space Science Center, Chinese Academy of Sciences, Beijing 100190, China
² College of Earth and Planetary Sciences, The University of Chinese Academy of Sciences, Beijing 101408, China
³ School of Physics and Astronomy, The University of Leicester, Leicester LE1 7RH, UK
⁴ Purple Mountain Observatory, Chinese Academy of Sciences, Nanjing 210023, China
* Correspondence: trsun@swl.ac.cn (T.S.); cw@swl.ac.cn (C.W.)

Abstract: With the advent of soft X-ray imaging enabling global magnetopause detection, it is critical to use reconstruction techniques to derive the 3-dimensional magnetopause location from 2-dimensional X-ray images. One of the important assumptions adopted by most techniques is that the direction with maximum soft X-ray emission is the tangent direction of the magnetopause, which has not been validated in observation so far. This paper analyzes a magnetospheric solar wind charge exchange (SWCX) soft X-ray event detected by XMM–Newton during relatively stable solar wind and geomagnetic conditions. The tangent direction of the magnetopause is determined by an empirical magnetopause model. Observation results show that the maximum SWCX soft X-ray intensity gradient tends to be the tangent of the magnetopause’s inner boundary, while the maximum SWCX soft X-ray intensity tends to be the tangent of the magnetopause’s outer boundary. Therefore, it is credible to use the assumption that the tangent direction of the magnetopause is the maximum SWCX soft X-ray intensity or its gradient when reconstructing the 3-dimensional magnetopause location. In addition, since these two maxima tend to be the inner and outer boundaries of the magnetopause, the thickness of magnetopause can also be revealed by soft X-ray imaging.

Keywords: solar wind charge exchange (SWCX); soft X-ray; magnetopause; tangent; X-ray imaging



Citation: Zhang, Y.; Sun, T.; Carter, J.A.; Liu, W.; Sembay, S.; Ji, L.; Wang, C. The Relationship between Solar Wind Charge Exchange Soft X-ray Emission and the Tangent Direction of Magnetopause in an XMM–Newton Event. *Magnetochemistry* **2023**, *9*, 88. <https://doi.org/10.3390/magnetochemistry9040088>

Academic Editor: Chao Shen

Received: 12 February 2023

Revised: 15 March 2023

Accepted: 18 March 2023

Published: 24 March 2023



Copyright: © 2023 by the authors. Licensee MDPI, Basel, Switzerland. This article is an open access article distributed under the terms and conditions of the Creative Commons Attribution (CC BY) license (<https://creativecommons.org/licenses/by/4.0/>).

1. Introduction

The magnetosphere is formed by the interaction between the solar wind and the Earth’s inherent magnetic field. The magnetospheric magnetic field can effectively prevent the solar wind plasma from directly entering the magnetosphere, thus forming a boundary layer with rapidly changing plasma density, called the magnetopause. Studies on the magnetopause structure are mainly based on the magnetopause crossing event of satellites, which is judged by the sudden changes of plasma and field detected in situ. Due to the limitation of sparse in situ detections, it is not sufficient to study the global response of large-scale magnetopause to solar wind disturbances.

Recently, a new method is being developed to remotely observe the large-scale structure of magnetopause by using soft X-ray imaging [1–4]. This method is based on the solar wind charge exchange (SWCX) process, which will produce soft X-rays [5]. When the high-valence ion (such as O^{7+} and O^{8+}) in the solar wind interacts with the neutral component (mainly neutral hydrogen atoms) in the Earth’s space, the ion gets an electron and enters the excited state. Then the excited ion returns to the ground state by emitting photons in the soft X-ray band. As the solar wind cannot pass directly through the magnetopause, the magnetosphere is “dark” in the soft X-ray band. As the magnetosheath is

the region where the solar wind ion density is enhanced after the deceleration of the bow shock, the magnetosheath is “bright” in the soft X-ray band. As the cusp regions are two special regions on the magnetopause where the solar wind can directly enter the near-Earth space, the cusp regions are also “bright” in the soft X-ray band. Therefore, a sharp change boundary of soft X-ray emissivity is formed near the magnetopause. It means that the large-scale structure of magnetopause can be revealed from the X-ray images.

After the soft X-ray generated by SWCX was first observed on the comet [6], it has been widely observed on Earth [7], Jupiter [8], Mars [9], Venus [10], the moon [11] and the heliosphere [12]. At present, observations of SWCX soft X-ray in the Earth’s magnetosheath are all from astronomical X-ray satellites, whose field of view is very narrow, so it is impossible to image the entire magnetosphere [7,13–28]. Based on this, the Chinese Academy of Sciences (CAS) and the European Space Agency (ESA) proposed the joint space science satellite program: Solar wind Magnetospheric Ionosphere Link Explorer (SMILE). The Soft X-ray Imager (SXI) of SMILE has a unique wide field of view ($16^\circ \times 27^\circ$), and will creatively image the entire Earth’s magnetosheath and cusp regions in soft X-ray band. SMILE will be launched in 2024~2025 [29,30].

For future magnetospheric imaging missions such as SMILE, how to reconstruct the 3-dimensional (3D) magnetopause structure from 2-dimensional (2D) soft X-ray images is of great significance. Wang and Sun [31] summarized four reconstruction approaches of magnetopause location developed so far: Tangential Direction Approach (TDA; [32]), Boundary Fitting Approach (BFA; [33,34]), Tangent Fitting Approach (TFA; [35]), and Computed Tomography Approach (CTA; [36]). Because imaging loses one-dimensional information on the line of sight, it is necessary to introduce assumptions to reconstruct the 3D magnetopause structure from 2D soft X-ray images. In fact, 3D magnetopause reconstruction is a balance between the number of X-ray images needed and the assumptions needed. The more the number of X-ray images, the fewer assumptions need to be made in reconstruction. For example, the CTA method hardly needs to make any assumptions, but at the same time, a large number of X-ray images used must be obtained under the condition that the magnetosphere is basically unchanged. Therefore, the CTA method is only applicable to the long-term stability of the solar wind, or after the satellite has accumulated a large number of magnetospheric images in the long-term operation process. If the number of X-ray images is reduced to two, the TDA method can be used. If it is reduced to only one, the TFA method or BFA method can be used. The reduction in the number of X-ray images leads to the introduction of assumptions in all three methods. Among them, the TFA method and BFA method have almost no requirements for the X-ray image used, so they are applicable to almost any solar wind conditions, especially for the rapidly changing solar wind. Therefore, for most methods, it is necessary to introduce assumptions, and the validation of those assumptions will be essential to the determination of magnetopause location.

An important assumption made by the TDA and TFA approaches is that the direction with maximum X-ray intensity corresponds to the tangent direction of the magnetopause. This assumption is reasonable from the magnetohydrodynamic (MHD) point of view [32]. On the one hand, the neutral hydrogen density increases rapidly with the decrease of the distance from the Earth, so the X-ray emissivity near the magnetopause is usually the strongest. On the other hand, the tangent of the magnetopause is the direction that maximizes the path length through the strong X-ray emissivity region. Since the magnetopause has a certain thickness in MHD due to the numerical dissipation, Sun et al. [37] proposed that the magnetopause determined by using the maximum X-ray intensity tended to be closer to the outer boundary of the magnetopause, while the magnetopause determined by using the maximum X-ray intensity gradient was near the center or inner boundary of the magnetopause, using the Piecewise Parabolic Method with a Lagrangian remap (PPMLR) MHD simulation. Samsonov et al. [38] presented that the magnetopause was located near the maximum X-ray intensity gradient or between the maximum X-ray intensity and its gradient, and the maximum X-ray intensity could be used as an indicator of magnetopause’s

outer boundary, by using two MHD simulations: the Space Weather Modeling Framework (SWMF) and Lyon–Fedder–Mobarry (LFM). However, the relationship between SWCX soft X-ray emission and the tangent direction of magnetopause has not been validated in observation so far.

The X-ray intensity of magnetospheric SWCX emission is determined by the distribution of 3D X-ray emissivity and the path length during the integration process. The local X-ray emissivity is determined by solar wind density and velocity, neutral hydrogen density and SWCX efficiency factor. The integral path is determined by the satellite's line of sight and magnetopause's position which is affected by solar wind conditions. Thus, in order to study the relationship between SWCX soft X-ray emission and the tangent direction of the magnetopause, this paper selects a magnetospheric SWCX soft X-ray observation detected by XMM–Newton during relatively stable solar wind and geomagnetic conditions. The tangent direction of the magnetopause is determined by Lin's magnetopause model [39]. Section 2 introduces the methods, Section 3 describes the results, and Section 4 shows the conclusions.

2. Methods

2.1. XMM–Newton Data Analysis

XMM–Newton original data files (ODFs) were downloaded from the XMM–Newton science archive. The identifier (ID) of this observation is 0306700301, the astronomical observation target is DA530SE (20 h 53 m 20.00 s, +55d 13' 56.0", J2000), and the operation modes of all three X-ray cameras (MOS1, MOS2 and PN) are full frame mode. To analyze XMM–Newton data, this paper used the Science Analysis System (SAS) software (version 20.0.0) and the Current Calibration Files (CCFs) released on 25 October 2022.

After the initial data processing as described in the Appendix A, we selected the data within the 11.7 arc minutes radius region centered on the common sky position of the three cameras (20:53:18.0606, +55:13:56.005, J2000). Here, to remove the background signal from astronomical point sources, we used the point source lists available in the XMM–Newton science archive and excluded the data within the 35 arc seconds radius region centered on the position of each point source. Figure 1 shows the soft X-ray images of three cameras and the extraction region of X-ray signals, of which 47 astronomical point sources need to be removed. Finally, we selected data within the good time intervals (GTIs) which were not contaminated by soft protons. Since the feature of highly variable soft proton contamination is the significant increase of count rate, we used the SAS task *espfilt*. It performed a Gaussian fitting on the count rate's histogram and selected the time when the count rate was within the range of 1.5 sigma of the Gaussian peak's count rate as the GTIs. Figure 2 shows the count rate curves of three cameras and the available time for further analyzing X-ray signals that vary with time.

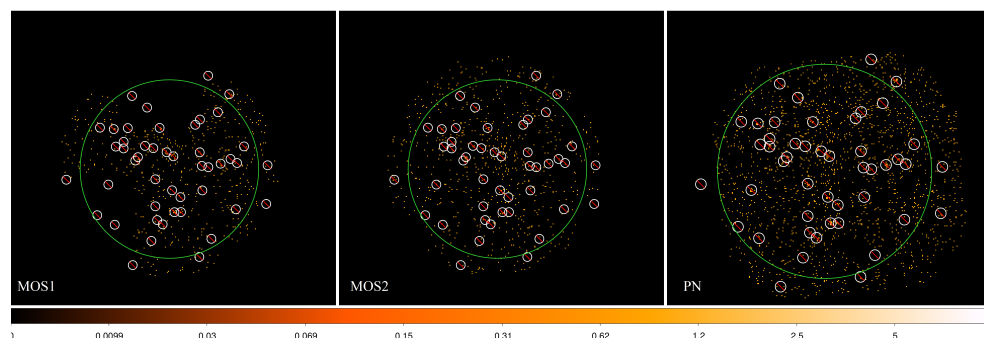


Figure 1. X-ray images of three cameras in 0.3–2.0 keV band. The green circle represents the extracted region of the X-ray signal. The small white circle with a red slash represents the region to be removed. CCD6 of MOS1 was damaged by the impact of a micrometeorite. Abnormal CCD4 of MOS1 was excluded.

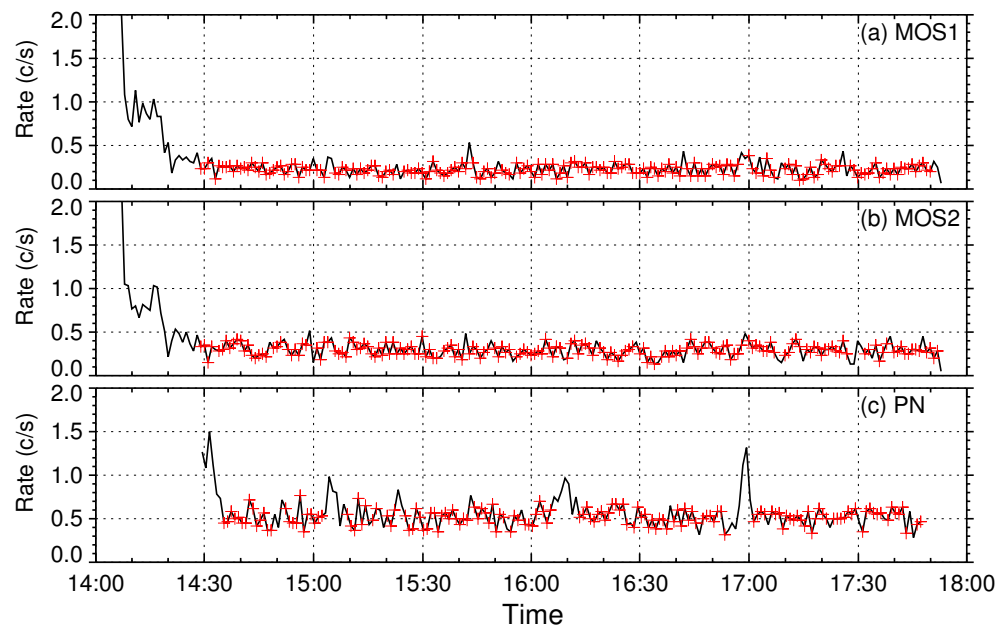


Figure 2. Count rate curves of three cameras in 2.5–8.5 keV band: (a) MOS1, (b) MOS2, (c) PN, where the red represents GTIs.

After the above steps, although the time-varying X-ray signal was obtained, it included not only magnetospheric SWCX emission but also other background signals, which were mainly composed of the cosmic X-ray background, particle background, heliospheric SWCX emission and residual soft proton contamination. As XMM–Newton is an astronomical satellite, its field of view is much smaller than that of magnetospheric imaging satellites such as SMILE. In this paper, the count rate of 0.5–0.7 keV band is used to characterize the X-ray intensity of magnetospheric SWCX emission [13,15]. SWCX in this band mainly comes from O^{7+} and O^{8+} in the solar wind, so it has the characteristics of high intensity and simple spectrum. In addition, the count rate of the 5.0–7.0 keV band is used to estimate the changes of other background signals, because this band is not affected by SWCX emission with energy mainly lower than 1 keV.

2.2. Lin's Magnetopause Model

The tangent direction of magnetopause is obtained by the empirical magnetopause model proposed by Lin et al. [39]. It is a 3D asymmetric magnetopause model developed for the corrected Geocentric Solar Magnetospheric (GSM) coordinates, which is parameterized by the solar wind dynamic pressure (P) and magnetic pressure, z component (B_z) of interplanetary magnetic field (IMF) and dipole tilt angle. In this paper, the angle (θ) between the observation direction of XMM–Newton and the tangent direction of magnetopause obtained by Lin's model is used to quantify the observational geometric relationship.

3. Results

3.1. Solar Wind and Geomagnetic Conditions

Figure 3 shows the solar wind and geomagnetic conditions from 11:00 to 21:00 on 19 April 2005. The available observation time of XMM–Newton is 14:30–17:53 (gray shadow). Solar wind plasma, IMF and geomagnetic activity index are 1-min data from OMNI, and solar wind ion abundance data is 1-h data from the Advanced Composition Explorer (ACE). The solar wind and geomagnetic conditions of this XMM–Newton event are relatively stable in three aspects. (1) The ion flux is relatively stable. As shown in Figure 3a,d, the average proton density, velocity, and density ratio of O^{7+} to O^{6+} (O^{7+}/O^{6+}) is 16.8 n/cc, 344.1 km/s, and 0.4, with a floating range of 16.4%, 1.9%, and 6.5%, respectively. Since the ionization state of ions is usually stabilized after leaving the Sun [40], the change of ion flux is estimated by proton flux and O^{7+}/O^{6+} . (2) The location of the

magnetopause is basically stable. As shown in Figure 3b,c, the average dynamic pressure is 4.0 nPa with a floating range of 19.5%, and all IMF components are between ± 5 nT. (3) The geomagnetic activities are quiet. As shown in Figure 3e,f, the AE index is always less than 300 nT, and the SYM/H index is between ± 5 nT, which indicates that neither magnetic substorm nor storm occurred during this observation, so the geomagnetic activity level is very low. In addition, the average proton density and the ionization state of ions are high, which is conducive to the study of magnetospheric SWCX emission, as the signal is strong enough not to be overwhelmed by other background signals [41]. To sum up, the solar wind and geomagnetic conditions of this XMM–Newton event are very suitable for studying the influence of observational geometric relationship to magnetospheric SWCX soft X-ray emission.

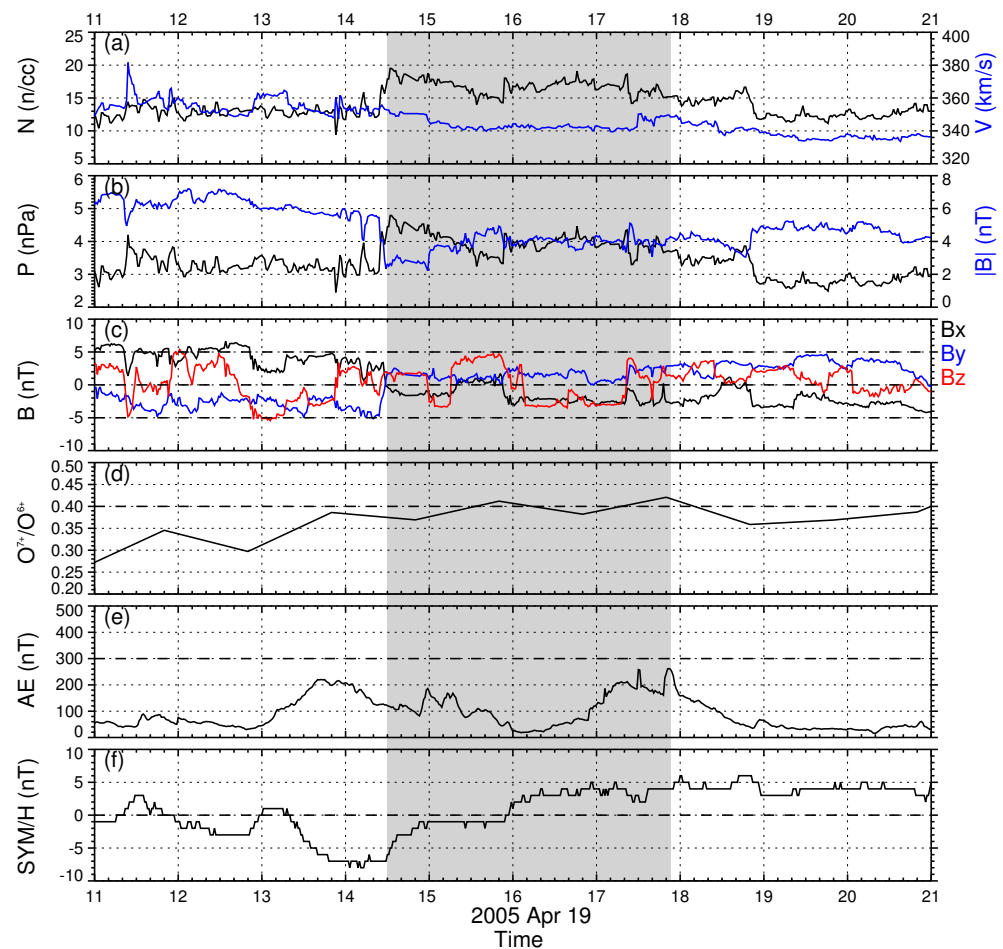


Figure 3. Solar wind conditions: (a) proton density (black) and velocity (blue), (b) dynamic pressure (black) and IMF (blue), (c) three components of IMF, (d) the density ratio of O^{7+} to O^{6+} . Geomagnetic activities: (e) AE index: the index describing the intensity of magnetic substorms in the polar region, (f) SYM/H index: the index describing the intensity of magnetic storm. Grey shadow is the time of XMM–Newton observation.

3.2. Line of Sight

Figure 4 shows XMM–Newton’s line of sight in the GSM coordinates. The location of the magnetopause is calculated from Lin’s model using the average solar wind conditions. As shown in the right panel (X–Z plane), as XMM–Newton gradually moves towards the upstream direction of the magnetopause (positive X direction), there are three observational geometric relationships between its line of sight and the magnetopause, first intersecting, then tangent and finally non-intersecting. As shown in the two panels, XMM–Newton’s line of sight is always near the subsolar of the magnetosphere with the strongest SWCX soft

X-ray emissivity. In addition, XMM–Newton is always located outside the magnetosphere, which is similar to the orbital position that magnetospheric soft X-ray imaging satellites such as SMILE will adopt in the future. To sum up, the line of sight of this XMM–Newton event is very suitable for studying the influence of observational geometric relationship to magnetospheric soft X-ray emission.

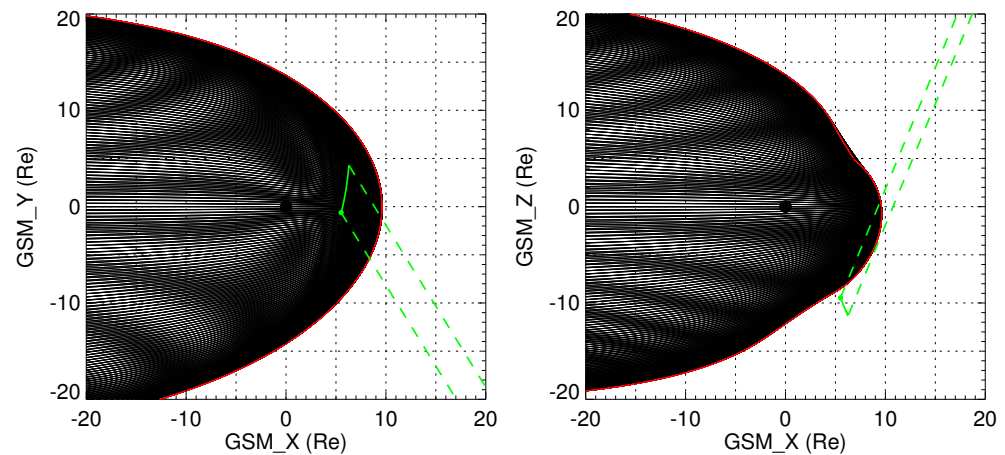


Figure 4. XMM–Newton’s line of sight in the GSM coordinates. The black ball represents the Earth, the shadow region represents the magnetosphere, and the red curve represents the magnetopause. The green curve is the orbital position of XMM–Newton, where the dot is the start time, and the dotted line extending from it is the observation direction.

3.3. SWCX Soft X-Ray Emission

Figure 5b,c show the 5-min SWCX soft X-ray emission observed by XMM–Newton. As shown in panel (b), by comparing the X-ray signal affected by both SWCX and other backgrounds (0.5–0.7 keV) and the X-ray signal only affected by other backgrounds (5.0–7.0 keV), the time corresponding to the maximum SWCX soft X-ray intensity is 16:29–16:39 (dark green shadow) and 17:34–17:44 (light green shadow). As shown in panel (c), by subtracting the gradient of the X-ray signal only affected by other backgrounds (5.0–7.0 keV) from the gradient of X-ray signal affected by both SWCX and other backgrounds (0.5–0.7 keV), the most likely time corresponding to the maximum SWCX soft X-ray intensity gradient is 15:54–15:59 (orange shadow). To sum up, the SWCX soft X-ray emission observed by XMM–Newton reached the maximum intensity gradient at 15:54–15:59, then reached the first maximum intensity at 16:29–16:39, and then continued to reach the second maximum intensity at 17:34–17:44.

3.4. Observational Geometric Relationship

In order to obtain the tangent direction of the magnetopause, a magnetopause model is necessary. In this paper, the empirical magnetopause model proposed by Lin et al. [39] was adopted. In order to verify the rationality of selecting Lin’s magnetopause model, we compared it with in situ satellite detection. Figure 6 shows the in situ detection data and orbital position of Geotail, as well as the magnetopause location calculated by Lin’s model. The location of magnetopause can usually be determined by the magnetopause crossing event of the satellite. When the satellite enters the magnetosphere from the magnetosheath, it is usually characterized by changes in the direction and/or magnitude of the magnetic field, changes in the plasma velocity decreases in the plasma density, and increases in the plasma temperature [39]. Although there was no in situ satellite crossing the magnetopause during the studied event, Geotail passed through the magnetopause at about 3:00 on April 19 (orange vertical line in the panels (a–c)), which was 11.5 h before the start of XMM–Newton observation. Meanwhile, Geotail (orange dot in the panel (d)) is just located at the magnetopause calculated by Lin’s model. In addition, this position happens to be near the tangent point of XMM–Newton’s line of sight and the magnetopause. Thus, it is credible

to adopt Lin's magnetopause model to obtain the time-varying observational geometric relationship between XMM-Newton's line of sight and magnetopause. As shown in the panel (d), the observational geometric relationship is quantified by the angle (θ) between the observation direction of XMM-Newton and the tangent direction of magnetopause obtained by Lin's model. When $\theta < 0$, it is intersected. When $\theta = 0$, it is tangent. When $\theta > 0$, it is disjoint.

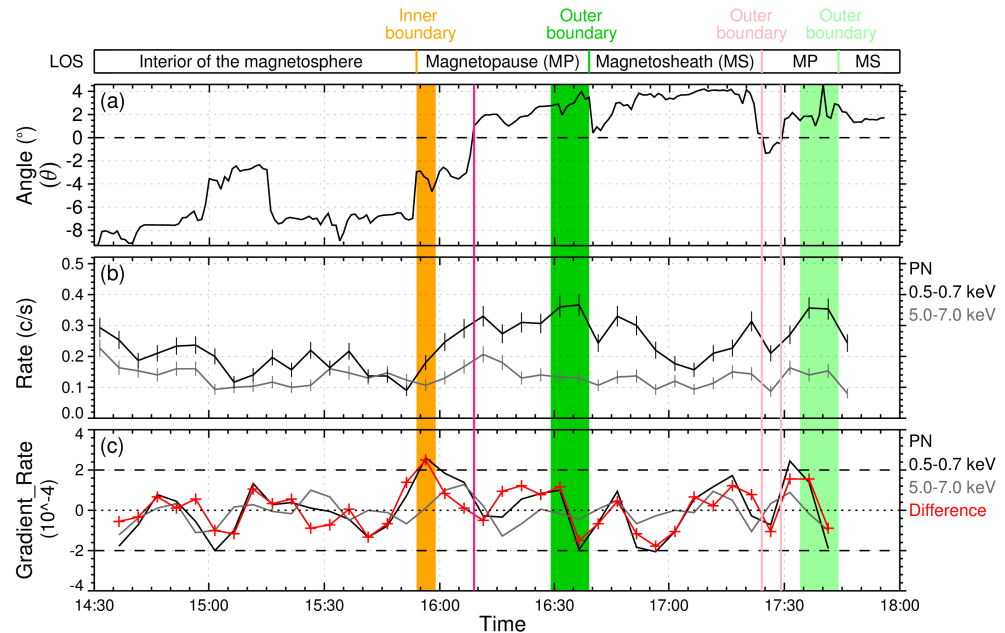


Figure 5. (a) The angle between the observation direction of XMM-Newton and the tangent direction of magnetopause obtained by Lin's model. (b) The count rate in the 0.5–0.7 keV (black) and 5.0–7.0 keV (gray) bands observed by XMM-Newton's PN camera (similar to MOS cameras). (c) The gradient of count rate in the 0.5–0.7 keV (black) and 5.0–7.0 keV (gray) band, and the difference between them (red). The region that XMM-Newton's line of sight passes through over time is displayed at the top.

Figure 5a shows the observational geometric relationship between XMM-Newton's line of sight and the magnetopause calculated by Lin's model. It is clear that XMM-Newton's line of sight is tangent to the magnetopause at 16:09 (dark pink vertical line), 17:24 and 17:29 (light pink vertical line). This seems to indicate that XMM-Newton's line of sight crossed the magnetopause twice. First, as XMM-Newton moved away from the earth, its line of sight moved from the interior of the magnetosphere to the magnetopause at 16:09. Secondly, XMM-Newton's line of sight briefly returned from the magnetosheath to the magnetopause during 17:24–17:29, which was due to the sudden decline of dynamic pressure and the shift of B_z from south to north, resulting in the magnetopause also moving away from the earth (as shown in Figure 3b,c).

3.5. Tangent Direction of Magnetopause

As shown in Figure 5, firstly, it is obvious that the time when the SWCX soft X-ray intensity reaches the maximum twice is later than the time when XMM-Newton's line of sight is tangent to the magnetopause. The first delay is about 30 min, and the second delay is about 20 min. Since the average moving speed of XMM-Newton in these two times is about 0.30 km/s and 0.42 km/s, respectively, the corresponding distances of these two delays are about 548.9 km and 502.2 km, respectively. Because the magnetopause is a boundary layer with a certain thickness, this delay reveals that the maximum SWCX soft X-ray intensity tends to be the tangent direction of magnetopause's outer boundary. Secondly, the most likely time when the SWCX soft X-ray intensity gradient reaches its maximum is about 15 min earlier than the time when XMM-Newton's line of sight is

tangent to the magnetopause. Since the average moving speed of XMM–Newton at this time is about 0.29 km/s, the corresponding distance of this advance is about 261.2 km. This advance may reveal that the maximum SWCX soft X-ray intensity gradient tends to be the tangent direction of magnetopause’s inner boundary. To sum up, this whole XMM–Newton observation event can be divided into three stages. (1) The line of sight moves from the interior of the magnetosphere to the magnetopause. When it is tangent to the inner boundary of the magnetopause, the SWCX soft X-ray intensity gradient reaches the maximum. (2) The line of sight moves from the magnetopause to the magnetosheath. When it is tangent to the outer boundary of the magnetopause, the SWCX soft X-ray intensity reaches the maximum. (3) The line of sight briefly returns to the magnetopause from the magnetosheath. When it is tangent to the inner boundary of magnetopause twice, the SWCX soft X-ray intensity also reaches the maximum twice.

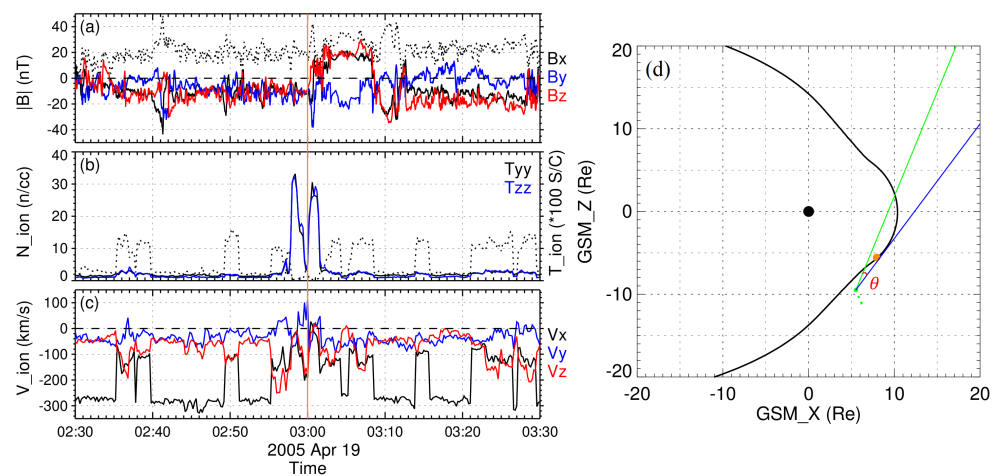


Figure 6. Geotail in situ detection data: (a) magnitude (dotted line) and three components of the magnetic field in the GSM coordinates, (b) ion density (dotted line) and two components of ion temperature in satellite coordinates, (c) three components of ion velocity in the GSM coordinates. Panel (d) shows the situation at 3:00 on April 19 in the GSM coordinates. The black curve represents the magnetopause calculated by Lin’s model. The orange dot represents the orbital position of Geotail. The green dotted line is the orbital position of XMM–Newton. The green line represents the observation direction of XMM–Newton. The blue line represents the tangent direction of the magnetopause. The angle between the two directions is marked as θ .

In summary, the maximum SWCX soft X-ray intensity gradient tends to be the tangent of the magnetopause’s inner boundary, while the maximum SWCX soft X-ray intensity tends to be the tangent of the magnetopause’s outer boundary. Based on this, the thickness of magnetopause at the tangent point (about 10h36m, -39° in the GSM coordinates) can be inferred as about 786.7 km (0.123 Re). The indication of magnetopause’s inner and outer boundaries revealed from the observation is consistent with the MHD simulation results of Sun et al. [37] and Samsonov et al. [38], which is reasonable because the thickness of magnetopause is greater than the spatial accuracy of MHD simulation of 0.1 Re. Therefore, for future magnetospheric soft X-ray imaging satellites such as SMILE, it is credible to use the assumption that the tangent direction of the magnetopause is the maximum SWCX soft X-ray intensity or its gradient when reconstructing the 3D magnetopause location from 2D X-ray images. In addition, since these two maxima tend to be the inner and outer boundaries of the magnetopause, the thickness of magnetopause can also be revealed by soft X-ray imaging.

4. Conclusions

This paper selects a magnetospheric SWCX soft X-ray observation detected by XMM–Newton during relatively stable solar wind and geomagnetic conditions to study the

relationship between SWCX emission and the tangent direction of the magnetopause. In order to determine the tangent direction of magnetopause, Lin's magnetopause model is adopted by comparing with in situ detection from Geotail. The observation results show that the maximum SWCX soft X-ray intensity gradient tends to be the tangent of the magnetopause's inner boundary, while the maximum SWCX soft X-ray intensity tends to be the tangent of the magnetopause's outer boundary. Therefore, for future magnetospheric soft X-ray imaging satellites such as SMILE, it is credible to use the assumption that the tangent direction of the magnetopause is the maximum SWCX soft X-ray intensity or its gradient when reconstructing the 3D magnetopause location from 2D X-ray images. In addition, since these two maxima tend to be the inner and outer boundaries of the magnetopause, the thickness of magnetopause can also be revealed by soft X-ray imaging.

Author Contributions: Conceptualization, C.W.; Methodology, T.S.; Software, Y.Z., J.A.C., W.L., S.S. and L.J.; Validation, Y.Z.; Formal analysis, Y.Z.; Investigation, Y.Z.; Data curation, Y.Z.; Writing—original draft, Y.Z.; Writing—review & editing, Y.Z., T.S., J.A.C., W.L., S.S., L.J. and C.W. All authors have read and agreed to the published version of the manuscript.

Funding: This work was supported by NNSFC grants 42188101 and 42074202; the Strategic Pioneer Program on Space Science, CAS Grant nos. XDA15350201, and in part by the Research Fund from the Chinese Academy of Sciences and the Specialized Research Fund for State Key Laboratories of China. Tianran Sun is also supported by the Young Elite Scientists Sponsorship Program (CAST - Y202045). Jennifer A. Carter is supported by Royal Society grant DHF\R1\211068.

Institutional Review Board Statement: Not applicable.

Informed Consent Statement: Not applicable.

Data Availability Statement: XMM–Newton data can be downloaded from <http://nxs.esac.esa.int/nxs-web/>. OMNI, ACE and Geotail data are available at <https://cdaweb.gsfc.nasa.gov/index.html>.

Acknowledgments: Thanks to the SMILE working group for the help and support.

Conflicts of Interest: The authors declare no conflict of interest.

Abbreviations

The following abbreviations are used in this manuscript:

SWCX Solar wind charge exchange
SMILE Solar wind Magnetospheric Ionosphere Link Explorer

Appendix A. Initial Data Processing

First, to generate the calibrated event lists from ODFs, we run SAS task `emproc` for MOS cameras and `epproc` task for PN camera. Secondly, to select X-ray events and remove noise pixels, we used the following standard filter expressions: $(PATTERN \leq 12) \&\& (\#XMMEA_EM)$ for MOS cameras, $(PATTERN == 0) \&\& (FLAG == 0)$ for PN camera. The *PATTERN* filter selects events in the entire X-ray library for MOS cameras, but only single-pixel events for pn camera. This selection optimizes the energy resolution of PN in the energy band less than 2 keV, which is the energy band of interested SWCX emission. The *#XMMEA_EM* filter of MOS removes events from known bright pixels or columns or areas close to the CCD boundary. The *FLAG == 0* filter of pn is more conservative than equivalent *#XMMEA_EP* filter, it not only removes the residual noise pixels, but also masks the adjacent areas of noise. Third, since the soft X-ray generated by SWCX is mainly below 1 keV and the background signal of some MOS CCD will be strongly enhanced in this energy band [42], to remove the data of those abnormal CCDs, we used the SAS task `emtaglenoise` for MOS cameras. As a result, the data from CCD4 of MOS1 was excluded.

References

1. Branduardi-Raymont, G.; Sembay, S.F.; Eastwood, J.P.; Sibeck, D.G.; Abbey, T.A.; Brown, P.; Carter, J.A.; Carr, C.M.; Forsyth, C.; Kataria, D.; et al. AXIOM: Advanced X-ray imaging of the magnetosphere. *Exp. Astron. Vol.* **2012**, *33*, 403–443. [[CrossRef](#)]
2. Collier, M.; Porter, F.; Sibeck, D.; Carter, J.; Chiao, M.; Chornay, D.; Cravens, T.; Galeazzi, M.; Keller, J.; Koutroumpa, D.; et al. Prototyping a global soft X-ray imaging instrument for heliophysics, planetary science, and astrophysics science. *Astron. Nachrichten* **2012**, *333*, 378–382. [[CrossRef](#)]
3. Walsh, B.M.; Collier, M.R.; Kuntz, K.D.; Porter, F.S.; Sibeck, D.G.; Snowden, S.L.; Carter, J.A.; Collado-Vega, Y.; Connor, H.K.; Cravens, T.E.; et al. Wide field-of-view soft X-ray imaging for solar wind-magnetosphere interactions. *J. Geophys. Res. Space Phys.* **2016**, *121*, 3353–3361. [[CrossRef](#)]
4. Sibeck, D.G.; Allen, R.; Aryan, H.; Bodewits, D.; Brandt, P.; Branduardi-Raymont, G.; Brown, G.; Carter, J.A.; Collado-Vega, Y.M.; Collier, M.R.; et al. Imaging Plasma Density Structures in the Soft X-Rays Generated by Solar Wind Charge Exchange with Neutrals. *Space Sci. Rev.* **2018**, *214*, 79. [[CrossRef](#)]
5. Cravens, T.E. Comet Hyakutake x-ray source: Charge transfer of solar wind heavy ions. *Geophys. Res. Lett.* **1997**, *24*, 105–108. [[CrossRef](#)]
6. Lisse, C.M.; Dennerl, K.; Englhauser, J.; Harden, M.; Marshall, F.E.; Mumma, M.J.; Petre, R.; Pye, J.P.; Ricketts, M.J.; Schmitt, J.; et al. Discovery of X-ray and Extreme Ultraviolet Emission from Comet C/Hyakutake 1996 B2. *Science* **1996**, *274*, 205–209. [[CrossRef](#)]
7. Wargelin, B.J.; Markevitch, M.; Juda, M.; Kharchenko, V.; Edgar, R.; Dalgarno, A.A. Chandra observations of the “dark” Moon and geocoronal solar wind charge transfer. *Astrophys. J.* **2004**, *607*, 596–610. [[CrossRef](#)]
8. Branduardi-Raymont, G.; Elsner, R.F.; Gladstone, G.R.; Ramsay, G.; Rodriguez, P.; Soria, R.; Waite, J.H. First observation of Jupiter by XMM–Newton. *A&A* **2004**, *424*, 331–337. [[CrossRef](#)]
9. Dennerl, K.; Lisse, C.M.; Bhardwaj, A.; Burwitz, V.; Englhauser, J.; Gunell, H.; Holmström, M.; Jansen, F.; Kharchenko, V.; Rodriguez-Pascual, P.M. First observation of Mars with XMM–Newton–High resolution X-ray spectroscopy with RGS. *A&A* **2006**, *451*, 709–722. [[CrossRef](#)]
10. Dennerl, K. X-rays from Venus observed with Chandra. *Planet. Space Sci.* **2008**, *56*, 1414–1423. [[CrossRef](#)]
11. Collier, M.R.; Snowden, S.L.; Sarantos, M.; Benna, M.; Carter, J.A.; Cravens, T.E.; Farrell, W.M.; Fatemi, S.; Hills, H.K.; Hodges, R.R.; et al. On lunar exospheric column densities and solar wind access beyond the terminator from ROSAT soft X-ray observations of solar wind charge exchange. *J. Geophys. Res. Planets* **2014**, *119*, 1459–1478. [[CrossRef](#)]
12. Galeazzi, M.; Chiao, M.; Collier, M.R.; Cravens, T.; Koutroumpa, D.; Kuntz, K.D.; Lallement, R.; Lepri, S.T.; McCammon, D.; Morgan, K.; et al. The origin of the local 1/4-keV X-ray flux in both charge exchange and a hot bubble. *Nature* **2014**, *512*, 171–173. [[CrossRef](#)] [[PubMed](#)]
13. Snowden, S.L.; Collier, M.R.; Kuntz, K.D. XMM–Newton Observation of Solar Wind Charge Exchange Emission. *Astrophys. J.* **2004**, *610*, 1182–1190. [[CrossRef](#)]
14. Fujimoto, R.; Mitsuda, K.; McCammon, D.; Takei, Y.; Bauer, M.; Ishisaki, Y.; Porter, F.S.; Yamaguchi, H.; Hayashida, K.; Yamasaki, N.Y. Evidence for Solar-Wind Charge-Exchange X-Ray Emission from the Earth’s Magnetosheath. *Prog. Theor. Phys. Suppl.* **2007**, *169*, 71–74. [[CrossRef](#)]
15. Carter, J.A.; Sembay, S. Identifying XMM–Newton observations affected by solar wind charge exchange. Part I. *A&A* **2008**, *489*, 837–848. [[CrossRef](#)]
16. Kuntz, K.D.; Snowden, S.L. The X-Ray-Emitting Components toward $l = 111^\circ$: The Local Hot Bubble and Beyond. *Astrophys. J.* **2008**, *674*, 209–219. [[CrossRef](#)]
17. Snowden, S.L.; Collier, M.R.; Cravens, T.; Kuntz, K.D.; Lepri, S.T.; Robertson, I.; Tomas, L. Observation of solar wind charge exchange emission from exospheric material in and outside Earth’s magnetosheath 2008 september 25. *Astrophys. J.* **2009**, *691*, 372. [[CrossRef](#)]
18. Carter, J.A.; Sembay, S.; Read, A.M. A high charge state coronal mass ejection seen through solar wind charge exchange emission as detected by XMM–Newton. *Mon. Not. R. Astron. Soc.* **2010**, *402*, 867–878. [[CrossRef](#)]
19. Ezoe, Y.; Ebisawa, K.; Yamasaki, N.Y.; Mitsuda, K.; Yoshitake, H.; Terada, N.; Miyoshi, Y.; Fujimoto, R. Time Variability of the Geocoronal Solar-Wind Charge Exchange in the Direction of the Celestial Equator. *Publ. Astron. Soc. Jpn.* **2010**, *62*, 981–986. [[CrossRef](#)]
20. Carter, J.A.; Sembay, S.; Read, A.M. Identifying XMM–Newton observations affected by solar wind charge exchange—Part II. *A&A* **2011**, *527*, A115. [[CrossRef](#)]
21. Ezoe, Y.; Miyoshi, Y.; Yoshitake, H.; Mitsuda, K.; Terada, N.; Oishi, S.; Ohashi, T. Enhancement of Terrestrial Diffuse X-Ray Emission Associated with Coronal Mass Ejection and Geomagnetic Storm. *Publ. Astron. Soc. Jpn.* **2011**, *63*, S691–S704. [[CrossRef](#)]
22. Carter, J.; Sembay, S.; Read, A. Exospheric solar wind charge exchange as seen by XMM–Newton. *Astron. Nachrichten* **2012**, *333*, 313–318. [[CrossRef](#)]
23. Ishikawa, K.; Ezoe, Y.; Miyoshi, Y.; Terada, N.; Mitsuda, K.; Ohashi, T. Suzaku Observation of Strong Solar-Wind Charge-Exchange Emission from the Terrestrial Exosphere during a Geomagnetic Storm. *Publ. Astron. Soc. Jpn.* **2013**, *65*, 63. [[CrossRef](#)]
24. Wargelin, B.J.; Kornbleuth, M.; Martin, P.L.; Juda, M. Observation and modeling of geocoronal charge exchange X-ray emission during solar wind gusts. *Astrophys. J.* **2014**, *796*, 28. [[CrossRef](#)]

25. Kuntz, K.D.; Collado-Vega, Y.M.; Collier, M.R.; Connor, H.K.; Cravens, T.E.; Koutroumpa, D.; Porter, F.S.; Robertson, I.P.; Sibeck, D.G.; Snowden, S.L.; et al. The solar wind charge-exchange production factor for Hydrogen. *Astrophys. J.* **2015**, *808*, 143. [[CrossRef](#)]
26. Ishi, D.; Ishikawa, K.; Numazawa, M.; Miyoshi, Y.; Terada, N.; Mitsuda, K.; Ohashi, T.; Ezoe, Y. Suzaku detection of enigmatic geocoronal solar wind charge exchange event associated with coronal mass ejection. *Publ. Astron. Soc. Jpn.* **2019**, *71*, 23. [[CrossRef](#)]
27. Asakura, K.; Matsumoto, H.; Okazaki, K.; Yoneyama, T.; Noda, H.; Hayashida, K.; Tsunemi, H.; Nakajima, H.; Katsuda, S.; Ishi, D.; et al. Suzaku detection of solar wind charge exchange emission from a variety of highly ionized ions in an interplanetary coronal mass ejection. *Publ. Astron. Soc. Jpn.* **2021**, *73*, 504–518. [[CrossRef](#)]
28. Zhang, Y.; Sun, T.; Wang, C.; Ji, L.; Carter, J.A.; Sembay, S.; Koutroumpa, D.; Liu, Y.D.; Liang, G.; Liu, W.; et al. Solar Wind Charge Exchange Soft X-Ray Emissions in the Magnetosphere during an Interplanetary Coronal Mass Ejection Compared to Its Driven Sheath. *Astrophys. J. Lett.* **2022**, *932*, L1. [[CrossRef](#)]
29. Branduardi-Raymont, G.; Wang, G.C.; Escoubet, C.; Adamovic, M.; Agnolon, D.; Berthomier, M.; Carter, J.; Chen, W.; Colangeli, L.; Collier, M.; et al. SMILE definition study report (Red Book). In *SMILE Definition Study Report, European Space Agency, ESA/SCI*; 2018; pp. 1–86. [[CrossRef](#)]
30. Wang, C.; Branduardi-Raymont, G. Update on the ESA-CAS Joint Solar Wind Magnetosphere Ionosphere Link Explorer(SMILE)Mission. *Chin. J. Space Sci.* **2020**, *40*, 700–703. [[CrossRef](#)]
31. Wang, C.; Sun, T. Methods to derive the magnetopause from soft X-ray images by the SMILE mission. *Geosci. Lett.* **2022**, *9*, 30. [[CrossRef](#)]
32. Collier, M.R.; Connor, H.K. Magnetopause Surface Reconstruction From Tangent Vector Observations. *J. Geophys. Res. Space Phys.* **2018**, *123*, 10,189–10,199. [[CrossRef](#)]
33. Jorgensen, A.M.; Sun, T.; Wang, C.; Dai, L.; Sembay, S.; Wei, F.; Guo, Y.; Xu, R. Boundary Detection in Three Dimensions With Application to the SMILE Mission: The Effect of Photon Noise. *J. Geophys. Res. Space Phys.* **2019**, *124*, 4365–4383. [[CrossRef](#)]
34. Jorgensen, A.M.; Sun, T.; Wang, C.; Dai, L.; Sembay, S.; Zheng, J.; Yu, X. Boundary Detection in Three Dimensions With Application to the SMILE Mission: The Effect of Model-Fitting Noise. *J. Geophys. Res. Space Phys.* **2019**, *124*, 4341–4355. [[CrossRef](#)]
35. Sun, T.; Wang, C.; Connor, H.K.; Jorgensen, A.M.; Sembay, S. Deriving the Magnetopause Position from the Soft X-Ray Image by Using the Tangent Fitting Approach. *J. Geophys. Res. Space Phys.* **2020**, *125*, e2020JA028169. [[CrossRef](#)]
36. Jorgensen, A.M.; Xu, R.; Sun, T.; Huang, Y.; Li, L.; Dai, L.; Wang, C. A Theoretical Study of the Tomographic Reconstruction of Magnetosheath X-Ray Emissions. *J. Geophys. Res. Space Phys.* **2022**, *127*, e2021JA029948. [[CrossRef](#)]
37. Sun, T.R.; Wang, C.; Sembay, S.F.; Lopez, R.E.; Escoubet, C.P.; Branduardi-Raymont, G.; Zheng, J.H.; Yu, X.Z.; Guo, X.C.; Dai, L.; et al. Soft X-ray Imaging of the Magnetosheath and Cusps Under Different Solar Wind Conditions: MHD Simulations. *J. Geophys. Res. Space Phys.* **2019**, *124*, 2435–2450. [[CrossRef](#)]
38. Samsonov, A.; Carter, J.A.; Read, A.; Sembay, S.; Branduardi-Raymont, G.; Sibeck, D.; Escoubet, P. Finding Magnetopause Standoff Distance Using a Soft X-Ray Imager: 1. Magnetospheric Masking. *J. Geophys. Res. Space Phys.* **2022**, *127*, e2022JA030848. [[CrossRef](#)]
39. Lin, R.L.; Zhang, X.X.; Liu, S.Q.; Wang, Y.L.; Gong, J.C. A three-dimensional asymmetric magnetopause model. *J. Geophys. Res. Space Phys.* **2010**, *115*, A04207. [[CrossRef](#)]
40. Lepri, S.T.; Landi, E.; Zurbuchen, T.H. Solar wind heavy ions over solar cycle 23: ACE/SWICS measurements. *Astrophys. J.* **2013**, *768*, 94. [[CrossRef](#)]
41. Guo, Y.; Sun, T.; Wang, C.; Sembay, S. Deriving the magnetopause position from wide field-of-view soft X-ray imager simulation. *Sci. China Earth Sci.* **2022**, *65*, 1601–1611. [[CrossRef](#)]
42. Kuntz, K.D.; Snowden, S.L. The EPIC-MOS particle-induced background spectra. *A&A* **2008**, *478*, 575–596. [[CrossRef](#)]

Disclaimer/Publisher's Note: The statements, opinions and data contained in all publications are solely those of the individual author(s) and contributor(s) and not of MDPI and/or the editor(s). MDPI and/or the editor(s) disclaim responsibility for any injury to people or property resulting from any ideas, methods, instructions or products referred to in the content.